



Cite as  
Nano-Micro Lett.  
(2020) 12:115

Received: 7 March 2020  
Accepted: 22 April 2020  
© The Author(s) 2020

# Intercalating Ultrathin MoO<sub>3</sub> Nanobelts into MXene Film with Ultrahigh Volumetric Capacitance and Excellent Deformation for High-Energy-Density Devices

Yuanming Wang<sup>1</sup>, Xue Wang<sup>1</sup>, Xiaolong Li<sup>1</sup>, Rong Liu<sup>2</sup> ✉, Yang Bai<sup>1</sup>, Huanhao Xiao<sup>1</sup>, Yang Liu<sup>1</sup>, Guohui Yuan<sup>1</sup> ✉

Yuanming Wang and Xue Wang have contributed equally to this work.

✉ Rong Liu, 562204852@qq.com; Guohui Yuan, yghhit@163.com

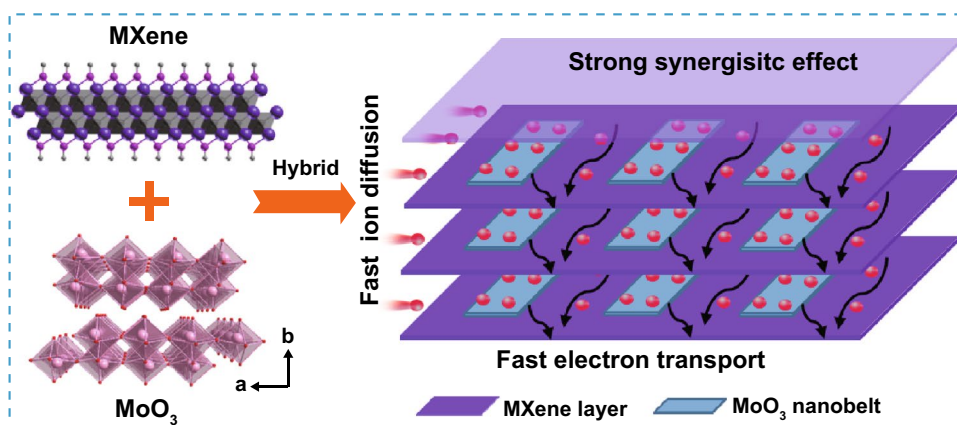
<sup>1</sup> MIIT Key Laboratory of Critical Materials Technology for New Energy Conversion and Storage, School of Chemistry and Chemical Engineering, Harbin Institute of Technology, No. 92 West Dazhi Street, Harbin 150001, People's Republic of China

<sup>2</sup> Ocean College, Hebei Agricultural University, No. 52 east section, Hebei Street, Qinhuangdao 066000, People's Republic of China

## HIGHLIGHTS

- All-pseudocapacitive and highly deformable MXene hybrid film is successfully fabricated by a facile and efficient vacuum-assisted filtration of ultrathin MoO<sub>3</sub> nanobelts and delaminated MXene nanosheets.
- The optimal M/MoO<sub>3</sub> hybrid electrode delivers an ultrahigh volumetric capacitance of 1817 F cm<sup>-3</sup> (545 F g<sup>-1</sup>), which exceeds large majority of previously reported MXene-based flexible electrodes.
- The symmetric supercapacitor presents excellent energy density of 44.6 Wh L<sup>-1</sup> (13.4 Wh kg<sup>-1</sup>), indicating the electrode promising in achieving high-energy-density devices.

**ABSTRACT** The restacking hindrance of MXene films restricts their development for high volumetric energy density of flexible supercapacitors toward applications in miniature, portable, wearable or implantable electronic devices. A valid solution is construction of rational heterojunction to achieve a synergistic property enhancement. The introduction of spacers such as graphene, CNTs,



cellulose and the like demonstrates limited enhancement in rate capability. The combination of currently reported pseudocapacitive materials and MXene tends to express the potential capacitance of pseudocapacitive materials rather than MXene, leading to low volumetric capacitance. Therefore, it is necessary to exploit more ideal candidate materials to couple with MXene for fully expressing both potentials.

Published online: 22 May 2020



SHANGHAI JIAO TONG UNIVERSITY PRESS

Springer

Herein, for the first time, high electrochemically active materials of ultrathin  $\text{MoO}_3$  nanobelts are intercalated into MXene films. In the composites,  $\text{MoO}_3$  nanobelts not only act as pillaring components to prevent restacking of MXene nanosheets for fully expressing the MXene pseudocapacitance in acidic environment but also provide considerable pseudocapacitive contribution. As a result, the optimal M/ $\text{MoO}_3$  electrode not only achieves a breakthrough in volumetric capacitance ( $1817 \text{ F cm}^{-3}$  and  $545 \text{ F g}^{-1}$ ), but also maintains good rate capability and excellent flexibility. Moreover, the corresponding symmetric supercapacitor likewise shows a remarkable energy density of  $44.6 \text{ Wh L}^{-1}$  ( $13.4 \text{ Wh kg}^{-1}$ ), rendering the flexible electrode a promising candidate for application in high-energy-density energy storage devices.

**KEYWORDS** MXene;  $\text{MoO}_3$  nanobelts; Hybrid film; Ultrahigh volumetric capacitance; Supercapacitors

## 1 Introduction

Recently, MXene ( $\text{Ti}_3\text{C}_2\text{T}_x$ ) has attracted great attention in the field of electrochemical energy storage, especially supercapacitors, predominantly due to their unique physical and chemical properties [1–3]. MXene has the similar planar geometry structure as the graphene, while the features of large specific surface area, few atomic thickness and unwrinkled flat surface render MXene materials be easily proceeded into thin film with robust mechanical strength and excellent flexibility [4–6]. More importantly, benefiting from MXene abundant and modifiable surface-terminating moieties, the self-supporting MXene films fabricated by simple vacuum filtration of delaminated MXene nanosheet colloid can directly serve as the flexible supercapacitor electrodes because of not only their flexibility and mechanical stability but also remarkable volumetric capacitance [7–9]. This brings great opportunities to develop next-generation high volumetric energy density of flexible supercapacitors for applications in electronic devices toward the development trend of miniaturization, portability, wearability and biomedical implantation. However, similar to other 2D nanomaterials, MXene nanosheets are easy to aggregate and restack during electrode fabrication process, which seriously impedes rapid diffusion of electrolyte ions and influences the full use of active surface of the electrodes, thus resulting in limited specific volumetric capacitance especially at high rates [10, 11].

A valid route to solve the restacking hindrance of MXene materials is construction of heterojunction by taking both advantages of selected target materials which can provide one or few functions such as good electrical conductivity, abundant electrochemically active sites as well as interlayered pillaring component and MXene materials to achieve a synergistic property enhancement. For example, by assembling graphene and MXene into stacked 2D heterojunction,

the rate capability of MXene-based hybrid electrode was enhanced to some extent due to the metallic electrical conductivity of graphene and larger 2D open structure of MXene [12]. Besides, CNTs [13], cellulose [14], PVA (polyvinyl alcohol) [15] and the like have also been employed to fabricate hybrid electrodes with MXene. However, these space materials are low active or inactive in energy storage, and the capacitive performance of electrodes demonstrates limited enhancement. Moreover, based on the surface chemical properties, MXene can provide a particularly suitable 2D building platform for some pseudocapacitive materials such as transition metal oxide (TMO) and layered double hydroxide (LDH) [16, 17]. Nevertheless, arbitrarily grown arrays of plates or rods on MXene substrate face the problems of insufficient mutual contact, inefficient utilization of active materials and failed film forming, resulting in sacrificing electrode flexibility and volumetric capacitance. Furthermore, it has been acknowledged that MXene materials exhibit highest capacity in the acidic electrolytes, while many efforts around combination of pseudocapacitive materials and MXene are conducted in the neutral or alkaline electrolytes because of acidic erosion for many active materials [18, 19]. The mismatch of electrolyte would bring about low capacitive contribution of MXene in the electrodes. In other words, MXene predominantly provides the conductive substrate for hybrid electrodes, finally leading to low specific volumetric capacitance and difficult to acquire a breakthrough of  $1500 \text{ F cm}^{-3}$  reported in pristine MXene hydrogel film [3]. Therefore, to obtain high-performance electrode, it is necessary to exploit more ideal candidate materials to couple with MXene for fully expressing both potentials.

Pseudocapacitive material of  $\text{MoO}_3$  nanobelts shows promising potential for MXene films including simple preparation process, mechanical stability, high electrochemical reaction activity and, more importantly, high pseudocapacitance in acidic environment [20, 21]. Herein, for the first

time, M/MoO<sub>3</sub> hybrid films are fabricated by simple blending of MXene nanosheet suspension and MoO<sub>3</sub> nanobelt dispersion and then experiencing vacuum-assisted filtration process. In the composites, the synthesized MoO<sub>3</sub> nanobelts are ultrathin (~16 nm), which is beneficial for the sufficient contact with the conductive MXene substrates to reduce intrinsic resistance and exposing more electrochemically active sites for high capacitive behavior. Meanwhile, MoO<sub>3</sub> nanobelts serve as the effective interlayers between MXene nanosheets to prevent MXene restacking and render the capacitance of MXene be fully expressed. As a result, the M/MoO<sub>3</sub> hybrid electrode with MoO<sub>3</sub> mass fraction of 20% exhibits an ultrahigh volumetric capacitance up to 1817 F cm<sup>-3</sup> (545 F g<sup>-1</sup>) at a scan rate of 3 mV s<sup>-1</sup> in 1 M H<sub>2</sub>SO<sub>4</sub> electrolyte, which exceeds large majority of previously reported MXene-based electrode materials and maintains good rate capability (773 F cm<sup>-3</sup> at 200 mV s<sup>-1</sup>). Benefiting from the ultrathin feature of both MXene and MoO<sub>3</sub>, the hybrid film presents high deformation (bendable, twistable and even foldable). Moreover, symmetric supercapacitor can yield a volumetric energy density of 44.6 Wh L<sup>-1</sup> (13.4 Wh kg<sup>-1</sup>), which belongs to the excellent performance in comparison with previously reported MXene-based symmetric supercapacitors. The work provides a simple and feasible strategy to design and fabricate advanced MXene-based flexible electrode with both high electrochemical performance and good flexibility, showing great potential for application in future flexible and portable electronics.

## 2 Experimental Section

### 2.1 Preparation of Delaminated MXene Nanosheets

Briefly, 3.2 g of LiF (Aladdin, 99%) was dissolved into 40 mL of 9 M HCl aqueous solution and the solution was stirred with a magnetic Teflon stir bar for 5 min to dissolve the salt. Then 2 g of Ti<sub>3</sub>AlC<sub>2</sub> powders were slowly added to the above mixing solution and the reaction was kept for 48 h at 35 °C to etch the Al atoms in the Ti<sub>3</sub>AlC<sub>2</sub> phase. Subsequently, the mixture was washed five times at least by adding deionized water until the pH of the supernatant was close to 7. Delaminated MXene suspension (d-Ti<sub>3</sub>C<sub>2</sub>T<sub>x</sub>) was prepared by adding deionized water to black sediment settled

at the bottom of the centrifuge tube along with vigorous hand-shaking delamination process. After centrifugation at 3500 rpm for 1 h, the supernatant with a color of dark green was collected. The concentration of the MXene suspension was determined by decanting a certain known volume of the suspension into a vial and measuring the weight of the vial after drying.

### 2.2 Preparation of Ultrathin MoO<sub>3</sub> Nanobelts

0.96 g Mo powder was carefully added into 12.5 mL H<sub>2</sub>O<sub>2</sub> (30%) with vigorously stirring for about 1 h in an ice bath until the solution became light yellow. Then 10 g polyethylene glycol (PEG) was added into the above solution with continuously stirring for another 1 h. After this, the solution was transferred to a 30-mL Teflon-lined stainless steel autoclave to undergo a hydrothermal reaction at 150 °C for 12 h. When the mixture cooled down, the product was filtered and washed alternately three times with ethyl alcohol and deionized water. Finally, MoO<sub>3</sub> nanobelts were dispersed in a known volume of deionized water to obtain the MoO<sub>3</sub> nanobelts dispersion. The concentration of MoO<sub>3</sub> nanobelts dispersion was obtained by the same method as that of MXene suspension.

### 2.3 Preparation of Freestanding M/MoO<sub>3</sub> (Ti<sub>3</sub>C<sub>2</sub>T<sub>x</sub>/MoO<sub>3</sub>) Hybrid Films

Vacuum filtration method was employed to fabricate M/MoO<sub>3</sub> hybrid films. First, a certain volume of MoO<sub>3</sub> dispersion was dropwise added into MXene suspension under ultrasonication for 30 min to get a uniformly mixed solution of MXene nanosheets and MoO<sub>3</sub> nanobelts. Then, the mixed solution was filtered through a filter membrane (0.22 μm pore size). Finally, the freestanding M/MoO<sub>3</sub> hybrid films were formed by drying at room temperature and peeling off from the filter membrane. M/MoO<sub>3</sub> hybrid films with different MoO<sub>3</sub> mass fraction were prepared by increasing the ratio of MoO<sub>3</sub> to MXene materials. For comparison, the pure MXene film was also fabricated via the same procedure. The mass loading of all as-prepared electrodes was controlled at around 1 mg cm<sup>-2</sup>.

## 2.4 Characterization

The morphology and microstructure of the as-prepared samples were investigated using field emission scanning electron microscopy (FESEM, Merlin Compact), transmission electron microscopy (TEM, FEI TF30) and atomic force microscope (AFM, Bruker Instruments Dimension Icon). Energy-dispersive spectroscopy (EDX) was performed on an electron microscope at an accelerating voltage of 20 kV. Crystal structures of samples were examined using a powder X-ray diffractometer (XRD) with Cu K $\alpha$  radiation at a scan rate of 5° min<sup>-1</sup>.

## 2.5 Electrochemical Measurements

All electrochemical measurements were taken on the CHI660E electrochemical workstation and Neware battery testing system in 1 M H<sub>2</sub>SO<sub>4</sub> aqueous electrolyte at room temperature. The electrochemical performances of single electrodes were evaluated by the typical three-electrode test configuration, in which self-supporting films were used as work electrode, Ag/AgCl in saturated KCl was the reference electrode and overcapacitive activated carbon served as the counter electrode. The symmetric supercapacitors were assembled with two pieces of identical size of flexible M/MoO<sub>3</sub>-20% films separated by porous nonwoven fabric. The electrochemical impedance spectroscopy (EIS) was conducted within a frequency range from 100 kHz to 0.01 Hz at an amplitude of 5 mV. Cycling stability was measured by repeating the galvanostatic charge/discharge test for 5000 cycles at 30 mA cm<sup>-2</sup>. The gravimetric capacitance was obtained from the discharge portion of cyclic voltammetry (CV) curves through Eq. 1:

$$C_m = \frac{\int IdV}{mv\Delta V} \quad (1)$$

where  $I$  is the current (mA),  $V$  is the potential window (V),  $m$  is the mass of the active materials (mg) and  $v$  is the scan rate (mV s<sup>-1</sup>), respectively. The volumetric capacitance of film electrodes is calculated according to Eqs. 2 and 3:

$$C_V = \rho C_m \quad (2)$$

$$\rho = \frac{m}{Sd} \quad (3)$$

where  $S$  (cm<sup>-2</sup>) and  $d$  (cm) are the surface area and thickness of film electrode, respectively. The gravimetric and volumetric energy density ( $E_m$ ,  $E_V$ ) and power density ( $P_m$ ,  $P_V$ ) of symmetric devices are calculated according to Eqs. 4–8:

$$E_m = \frac{1}{2} CV^2 \quad (4)$$

$$P_m = \frac{E}{\Delta t} \quad (5)$$

$$\Delta t = \frac{V}{v} \quad (6)$$

$$E_V = \rho E_m \quad (7)$$

$$P_V = \rho P_m \quad (8)$$

## 3 Results and Discussion

### 3.1 Film Fabrication and Sample Characterization

Figure 1a schematically illustrates the preparation process of M/MoO<sub>3</sub> hybrid films. In a typical synthesis, few-layered Ti<sub>3</sub>C<sub>2</sub>T<sub>x</sub> MXene nanosheet colloidal suspension was synthesized by selectively etching bulk Ti<sub>3</sub>AlC<sub>2</sub> precursor in LiF and HCl mixed solution, followed by mildly hand-shaking exfoliation. MoO<sub>3</sub> nanobelts homogeneous dispersion was prepared by a facile one-step hydrothermal process, where Mo powder was served as the Mo source, H<sub>2</sub>O<sub>2</sub> was the oxidant and PEG (polyethylene glycol) played the role of the crystal growth template for ultrathin feature. Both MXene nanosheet and MoO<sub>3</sub> nanobelt dispersions show hydrophilic characteristics, which can be highly stable in aqueous media. And the mixture solution including MXene nanosheets and MoO<sub>3</sub> nanobelts shows good compatibility without any precipitate (Fig. S1). Through vacuum-assisted filtration process, M/MoO<sub>3</sub> hybrid films with MoO<sub>3</sub> mass percentage of 10%, 20% and 30% were successfully prepared, which was subsequently denoted as M/MoO<sub>3</sub>-10%, M/MoO<sub>3</sub>-20% and M/MoO<sub>3</sub>-30%, respectively.

TEM image reveals the morphology of the prepared MXene nanosheets which are thin, transparent and possess a lateral dimension of hundreds of nanometers, as illustrated in Fig. 1b. XRD pattern (Fig. 1c) was employed to characterize

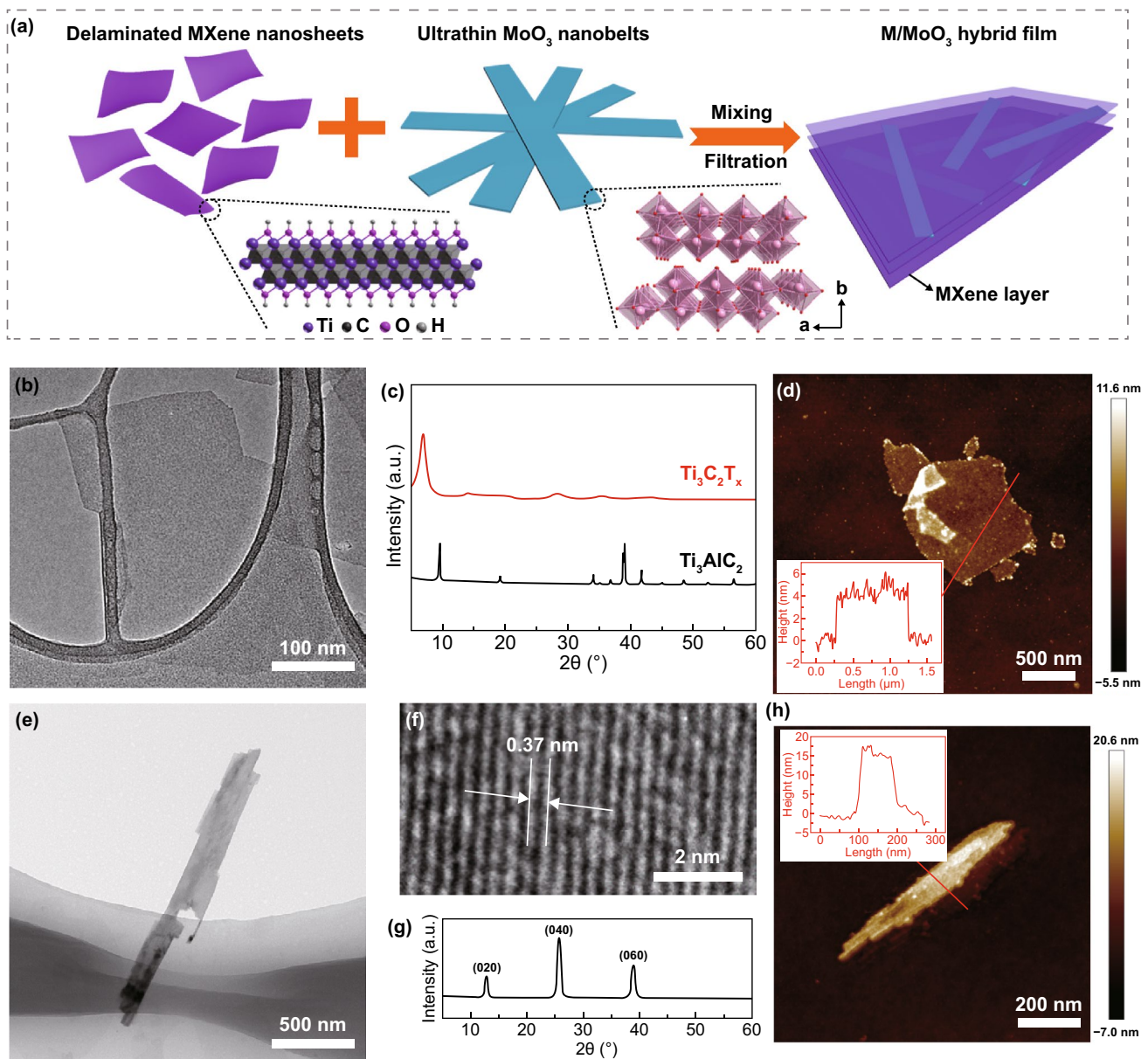


**Fig. 1** **a** Schematic illustration of the fabrication process of M/MoO<sub>3</sub> hybrid films, **b** TEM image of delaminated MXene nanosheets, **c** XRD patterns of the MAX (Ti<sub>3</sub>AlC<sub>2</sub>) precursor and the prepared delaminated MXene, **d** AFM image of MXene nanosheets. Inset shows the corresponding height profile along the lines in **d**, **e** TEM and **f** HR-TEM images of MoO<sub>3</sub> nanobelt, **g** XRD patterns of MoO<sub>3</sub> nanobelts, **h** AFM image of MoO<sub>3</sub> nanobelt. Inset shows the corresponding height profile along the lines in **h**

the structure and phase feature of MAX ceramic powders and delaminated MXene nanosheets. For Ti<sub>3</sub>C<sub>2</sub>T<sub>x</sub> MXene, the (002) diffraction peaks at 6.9° can be observed, which is in consistent with typical MXene with interlayered water molecules as reported in other studies [22]. From AFM characterization (Fig. 1d), the thickness of individual MXene nanosheets is close to 4 nm, demonstrating few-layered

MXene is synthesized as single layer of MXene flakes is about 1.5 nm [23]. MoO<sub>3</sub> morphology was investigated by SEM (Fig. S1) and TEM (Fig. 1e). The MoO<sub>3</sub> presents ribbonlike characteristics with a width of 100–200 nm and a length of 1–2 μm. The HR-TEM image (Fig. 1f) reveals the nanobelts with an interplanar spacing of 0.37 nm, which is consistent with the (002) *d*-spacing of α-MoO<sub>3</sub> [24].

Diffraction patterns are shown in Fig. 1g, which can be clearly indexed to be orthorhombic  $\text{MoO}_3$  (JCPDS No. 05-0508) [25, 26]. The strong diffraction peaks of (020), (040) and (060) reveal that the  $\text{MoO}_3$  nanobelts with a highly anisotropic growth own an obviously preferred orientation. Given that  $\alpha\text{-MoO}_3$  is constituted of stacking bilayer sheets of  $\text{MoO}_6$  octahedra with layered structure, the structure is favorable for the infiltration of small electrolyte ions for high capacitive behavior [27–29]. From AFM characterization (Fig. 1h), the height of  $\text{MoO}_3$  nanobelts is only around 16 nm which belongs to the ultrathin size in comparison with other literature reported ( $\sim 100$  nm) [24]. The ultrathin feature is not only beneficial for exposing more active sites for high pseudocapacitance, but also sufficient contact with the conductive substrates for fast electron transport.

Following the material characterizations, the morphology and microstructure of various  $\text{M}/\text{MoO}_3$  hybrid films and pure MXene film were investigated by scanning electron

microscopy. From the view of top SEM images as shown in Figs. 2a, b and S2a, b, pure MXene film is obviously smoother due to densely stacking of flat MXene nanosheets. After hybridization with  $\text{MoO}_3$ , it is found that these nanobelts are scattered in disorder and buried into the MXene substrates which provides continuous conductive networks for improving intrinsic conductivity of  $\text{MoO}_3$  nanobelts. The cross-sectional SEM images (Figs. 2c and S3a, b) indicate that  $\text{M}/\text{MoO}_3$  hybrid films maintain a well-aligned lamellar structure. Due to the insertion of nanobelts, the thickness of hybrid films gradually increases with the increasing mass percentage of  $\text{MoO}_3$  because the 2D face-to-face stacking of MXene nanosheets is the denser stacking mode in comparison with the nanobelt–nanosheet stacked structure. However, benefiting from the ultrathin structure of  $\text{MoO}_3$  nanobelts, the thickness increase is considerably limited in favor of achieving high volumetric performance. From the cross-sectional SEM images in high magnification (Fig. 2d),

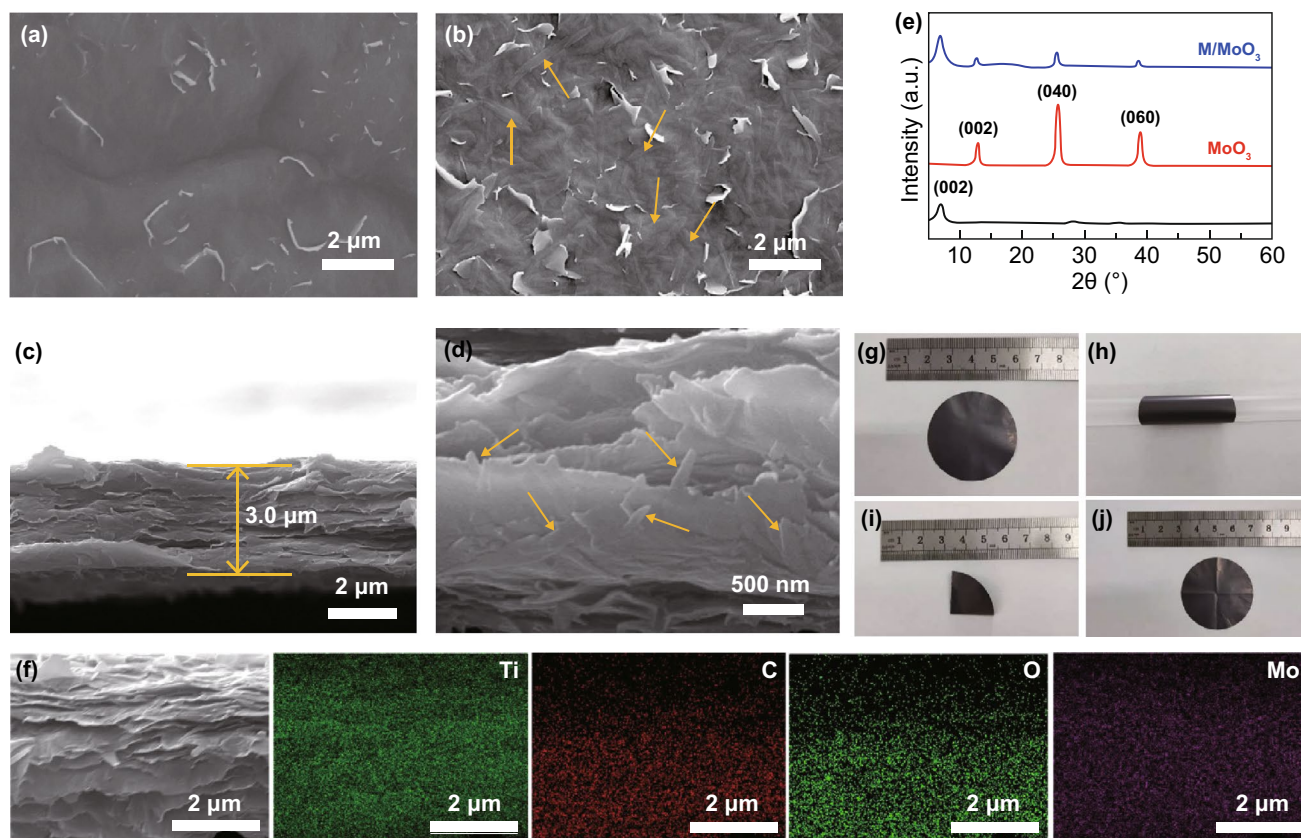


**Fig. 2** Top view SEM images of **a** pure MXene film and **b**  $\text{M}/\text{MoO}_3$ -20% hybrid film, **c**, **d** cross-sectional images of  $\text{M}/\text{MoO}_3$ -20% hybrid film, **e** XRD patterns of MXene film,  $\text{MoO}_3$  nanobelts and  $\text{M}/\text{MoO}_3$ -20% hybrid film, **f** EDX elemental mapping of Ti, C, O and Mo for the hybrid film, **g–j** Optical images of  $\text{M}/\text{MoO}_3$  hybrid film at different deformation status, which can be bended, rolled and even folded

MoO<sub>3</sub> nanobelts are inserted between the conductive MXene nanolayer, which is considered to be able to reduce the self-stacking problem of MXene nanosheets, thereby enlarging the accessible active surface for energy storage. Meanwhile, MXene could provide binding function for avoiding the active materials loss during the charging/discharging process. In addition, the M/MoO<sub>3</sub> hybrid film simultaneously exhibits the typical peaks of MXene and MoO<sub>3</sub> (Fig. 2e), indicating that the addition of MoO<sub>3</sub> nanobelts does not disturb the MXene stacking order along the *c* direction as a result of coexistence. The compositional distributions of M/MoO<sub>3</sub> hybrid film (Fig. 2f) were confirmed by elemental mapping analyses, in which homogeneous distributions of Ti, C, O and Mo elements are clearly showed within the M/MoO<sub>3</sub> hybrid film. Furthermore, the flexibility of electrodes is the significant assessment norms for flexible energy storage devices. As displayed in Fig. 2g–j, the M/MoO<sub>3</sub> hybrid film exhibits excellent flexibility and highly deformation, which can be curled around a glass rod and even be folded for many times, while no crack is found in the unfolded film. The tensile strength of hybrid films, as shown in Fig. S4, gradually decreases from 19.1 to 12.5 MPa with the addition of MoO<sub>3</sub> nanobelts, indicating that the structure of nanobelt–nanosheet stacked structure is relatively looser. Although the tensile strength of hybrid films is lower than that of pure MXene film (22.8 MPa), it still maintains a high level. This also indicates that MXene nanosheets and MoO<sub>3</sub> nanobelts are assembled tightly together, forming an integrated structure for high mechanical stability and flexibility.

### 3.2 Electrochemical Performance in a Three-Electrode System

The electrochemical performance of the as-prepared samples was investigated by using a three-electrode setup in 1 M H<sub>2</sub>SO<sub>4</sub> aqueous electrolyte in a potential window of –0.6 to 0.3 V. From CV profiles of the pure MXene (Fig. S5), a couple of broad redox peaks can be clearly observed, demonstrating that the capacitance mainly comes from the pseudocapacitance based on the reversible redox reaction along with the valence state change of the Ti atoms [30]. After the insertion of MoO<sub>3</sub> nanobelts, as illustrated in Figs. 3a and S6a, c, the CV curves of M/MoO<sub>3</sub> hybrid electrodes present an obvious difference from those of pure MXene electrode, which involves several pairs of new asymmetric redox peaks

at low scan rates, demonstrating MoO<sub>3</sub> provides pseudo-capacitive contribution for the hybrid electrodes. Although at a high scan rate of 100 mV s<sup>–1</sup>, there are obvious redox peaks of MoO<sub>3</sub> for these hybrid electrodes, indicating fast ion transport for faradaic reaction. Galvanostatic charge–discharge (GCD) profiles of these hybrid electrodes at various current densities are presented in Figs. 3b and S6b, d. All of them present a distortion from ideal triangle shape, where several pairs of charge/discharge plateaus are observed clearly for M/MoO<sub>3</sub> hybrid electrodes, indicating the pseudocapacitive nature, which is in good according with the results of CV curves. In Fig. 3c, a comparison of CV curves was made between pure MXene electrode and M/MoO<sub>3</sub> hybrid electrodes at a scan rate of 20 mV s<sup>–1</sup>. In comparison with pure MXene electrode, the M/MoO<sub>3</sub> hybrid electrodes exhibit a much higher CV integral area and the integral area gradually increases with the increasing mass percentage of MoO<sub>3</sub>, which is also in consistent with the results from GCD profiles (Fig. 3d), reflecting great improvement of the capacitance performance.

To better know the electrochemical behavior of electrodes, the capacitance of the MXene and M/MoO<sub>3</sub> electrodes were calculated from the CV curves in a wide scan rate range varying from 3 to 200 mV s<sup>–1</sup>, which is shown in Fig. 3e. Obviously, hybrid electrodes exhibit the higher specific capacitance over the whole range of scan rates in comparison with pure MXene electrode. And the specific capacitance of hybrid electrodes gradually rises with the increasing mass percentage of MoO<sub>3</sub>, demonstrating highly electrochemical active materials of MoO<sub>3</sub> in acidic electrolyte. At a low scan rate of 3 mV s<sup>–1</sup>, the hybrid electrodes deliver a high capacitance of 447, 545 and 580 F g<sup>–1</sup> corresponding to the samples of M/MoO<sub>3</sub>-10%, M/MoO<sub>3</sub>-20% and M/MoO<sub>3</sub>-30%, respectively, while the pure MXene electrode only yields a capacitance of 331 F g<sup>–1</sup> at the same scan rate. When the scan rate is increased up to 200 mV s<sup>–1</sup>, the hybrid electrodes still maintain 177 (M/MoO<sub>3</sub>-10%), 232 (M/MoO<sub>3</sub>-20%) and 249 F g<sup>–1</sup> (M/MoO<sub>3</sub>-30%), considerably higher than that of pure MXene electrode (124 F g<sup>–1</sup>). This indicates that the rate capability of hybrid electrodes does not drop off although large enhancement of capacitance performance in comparison with the pure MXene electrode. The greatly enhanced capacitive behavior is related to the structure of hybrid electrodes, where MoO<sub>3</sub> nanobelts not only serve as the interspacers of MXene to accelerate the in-time ion intercalation/extraction for fully expressing the MXene pseudocapacitance, but also are additional

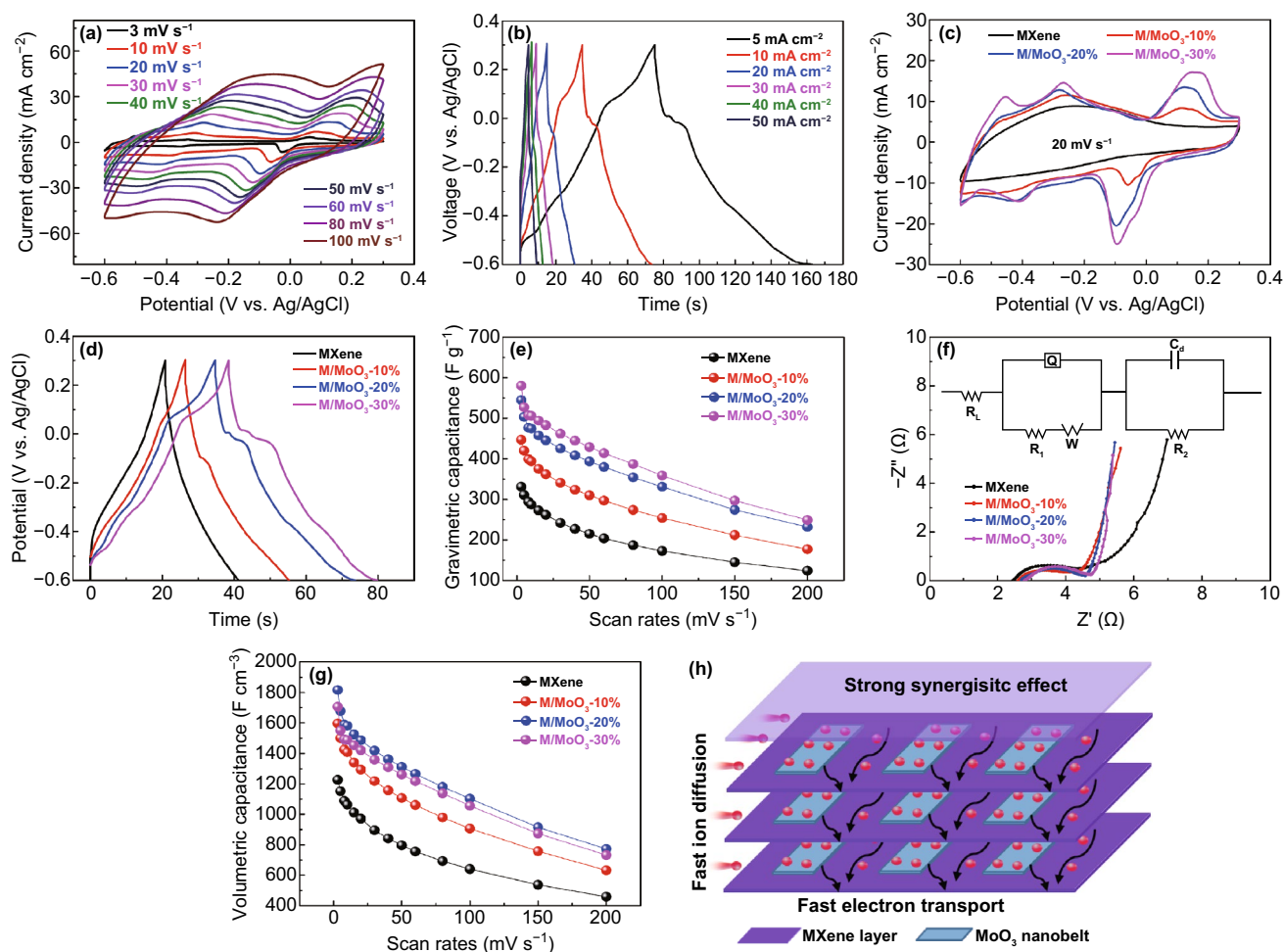


**Fig. 3** **a** CV curves of the M/MoO<sub>3</sub>-20% electrode at various scan rates, **b** GCD profiles of M/MoO<sub>3</sub>-20% electrode at various current densities, **c** CV curves of pure MXene and hybrid electrodes at a scan rate of 20 mV s<sup>-1</sup>, **d** GCD profiles of pure MXene and hybrid electrodes at a current density of 10 mA cm<sup>-2</sup>, **e** gravimetric specific capacitance of pure MXene and hybrid electrodes calculated from the CV curves of different scan rates, **f** Nyquist plots. Inset shows the equivalent circuit model for the Nyquist plots, **g** corresponding volumetric specific capacitance of various electrodes, **h** proposed schematic diagram of the high capacitive behavior from strong synergistic effect

electrochemically active materials for the improvement of whole capacitance. Electrochemical impedance spectroscopy (EIS) was further performed to study understand the kinetics of electrode processes. As shown in Fig. 3f, all of Nyquist plots consist of a quasi-semicircle in the high-frequency regions and a nearly vertical line in the low-frequency regions. In the high-frequency section, the semicircle arc presents the charge transfer resistance ( $R_{ct}$ ) and electrode surface properties. According to the equal circuit fitting (Fig. 3f inset), the  $R_{ct}$  value of pure MXene electrode is 2.2  $\Omega$ , while the hybrid electrodes show less diameter of semicircle arc which is 1.6, 1.8 and 2.0  $\Omega$  corresponding to the M/MoO<sub>3</sub>-10%, M/MoO<sub>3</sub>-20% and M/MoO<sub>3</sub>-30%, respectively. This might be due to

that ionic conductivity of M/MoO<sub>3</sub> electrodes is improved after embedding MoO<sub>3</sub> nanobelts for fast charge transfer.

In the aspect of volumetric performance, as shown in Fig. 3g, M/MoO<sub>3</sub>-20% hybrid electrode yields the highest capacitance. The highest volumetric capacitance can reach 1817 F cm<sup>-3</sup> at 3 mV s<sup>-1</sup>, much better than that of pure MXene (1225 F cm<sup>-3</sup>), approximately 1.5 times enhancement. Even at a high scan rate of 200 mV s<sup>-1</sup>, the volumetric capacitance can maintain 773 F cm<sup>-3</sup> in sharp comparison with that of pure MXene electrode (459 F cm<sup>-3</sup>). Nevertheless, the M/MoO<sub>3</sub>-30% electrode displays reduced volumetric capacitance than that of M/MoO<sub>3</sub>-20% electrode, because the continuous addition of MoO<sub>3</sub> will

visibly augment the thickness of hybrid electrode inevitably (Fig. S3), detriment of not only the improvement of volumetric performance but also the deterioration of flexibility to some extent. In order to comprehensively understand the great enhancement of volumetric performance of M/MoO<sub>3</sub>-20% electrode, schematic diagram of the proposed synergistic effect is presented in Fig. 3h and could be explained from the following aspects. Firstly, according to the above electrochemical analysis, both of MXene and MoO<sub>3</sub> show pseudocapacitive feature in acidic electrolyte in the potential of -0.6–0.3 V. MXene can not only lower the intrinsic resistance of MoO<sub>3</sub> nanobelts for fast electron transport in favor of achieving good rate capability, but also serve as the flexible substrate for MoO<sub>3</sub> materials which cannot act as self-supporting film electrode directly without slurry mixing method or conductive substrate due to bad mechanical stability and conductivity. Given that MoO<sub>3</sub> nanobelts distributed over the surface and interlamination of the MXene nanosheets, electrolyte ions are easily accessible to active surface including those of MoO<sub>3</sub> nanobelts and MXene nanosheets, thereby contributing to high capacitive behavior. And the ultrathin feature of MoO<sub>3</sub> nanobelts is beneficial for the improvement of volumetric performance in a certain range due to little increase in film thickness. But high mass percentage of MoO<sub>3</sub> nanobelts will lead to the increase in the film thickness which is unfavorable to the continuous increase in the volumetric capacitance. Therefore, the high volumetric capacitance of optimal M/MoO<sub>3</sub>-20% electrode is from the good synergistic effect of the two materials. As a result, the outstanding volumetric feature of M/MoO<sub>3</sub>-20% electrode with excellent flexibility renders it most promising in achieving high volumetric energy density of flexible energy storage device.

The electrochemical kinetics of M/MoO<sub>3</sub>-20% electrode was evaluated through Trasatti analysis method which is used to quantify the stored charges ( $q$ ) during the energy storage process. The total amount of stored charge ( $q_T$ ) consists of both outer ( $q_o$ ) and inner surface charges ( $q_i$ ), and they can be individually obtained by extrapolation of  $q$  to  $v=0$  and  $v \rightarrow \infty$ . The relevant formulas are as follows (Eqs. 9–11):

$$q_T = q_i + q_o \quad (9)$$

$$q = q_\infty + \kappa v^{-1/2} \quad (10)$$

$$\frac{1}{q} = \frac{1}{q_\infty} + \frac{v^{1/2}}{\kappa} \quad (11)$$

since the charge storage of the outer surface is a nondiffusion-controlled process, independent of scan rate, so  $q_o$  can be obtained from the extrapolation of  $q$  to  $v \rightarrow \infty$  by using Eq. 10, where  $q_o$  is equaled to  $q_\infty$ , and the result of the linear fitting is shown in Fig. 4a. At the inner surface, the charge storage is opposite, controlled by ion diffusion. The total charge ( $q_T$ ) can be obtained from the extrapolation of  $q$  to  $v=0$  by Eq. 11 and the result of the linear fitting is shown in Fig. 4b. As a consequence, the outer and total charges of M/MoO<sub>3</sub>-20% electrode are calculated to be 1141 and 1818 C cm<sup>-3</sup>, respectively. At the scan rate of 3 mV s<sup>-1</sup>, the practical charge storage calculated is 1635 C cm<sup>-3</sup>, which accounts for 90% of the total charge storage ( $q_T$ ), indicating high electrochemical utilization of M/MoO<sub>3</sub>-20% electrode during the charge/discharge process. The result means that most of the active surfaces are accessible to electrolyte ions. Cycling stability is also an important factor for evaluating the performance of electrode materials for supercapacitors in practical applications. The cycling stability of the M/MoO<sub>3</sub>-20% electrode was conducted by using GCD at a current density of 30 mA cm<sup>-2</sup> for 5000 cycles as provided in Fig. 4c. It can be seen that 100% of its initial specific capacitance is retained after continuous charging/discharging process, indicating good long-term cycle stability. This good stability might be associated with the tight laminar structure, where active materials are spatially defined in the interlayers for avoiding loss into the electrolyte. Comparison of the maximum volumetric capacitance and gravimetric capacitance of M/MoO<sub>3</sub>-20% electrode with other MXene-based state-of-the-art electrodes was made, which is depicted in Fig. 4d and Table S1. It is worth pointing out that, especially outstanding in terms of volumetric capacitance (1817 F cm<sup>-3</sup> obtained in 1 M H<sub>2</sub>SO<sub>4</sub> aqueous electrolyte), our electrode outperforms large majority of previously reported MXene-based flexible electrodes, such as MXene hydrogel (1500 F cm<sup>-3</sup>) [3], MXene/graphene (1040 F cm<sup>-3</sup>) [12], Ti<sub>3</sub>C<sub>2</sub>T<sub>x</sub>/SWCNT (390 F cm<sup>-3</sup>) [13], Ti<sub>3</sub>C<sub>2</sub>T<sub>x</sub>/MnO<sub>2</sub> (1025 F cm<sup>-3</sup>) [18], Ti<sub>3</sub>C<sub>2</sub>T<sub>x</sub> clay (900 F cm<sup>-3</sup>) [31], PPy/Ti<sub>3</sub>C<sub>2</sub>T<sub>x</sub> (1000 F cm<sup>-3</sup>) [32], MXene/CNTs (1083 F cm<sup>-3</sup>) [33], Ultracompact d-Ti<sub>3</sub>C<sub>2</sub> (633 F cm<sup>-3</sup>) [34] and M<sub>x</sub>P<sub>x</sub> fiber (614.5 F cm<sup>-3</sup>) [35].

### 3.3 Electrochemical Performance in a Symmetric Device

In order to further evaluate the feasibility of the hybrid electrode in practical application for flexible energy storage

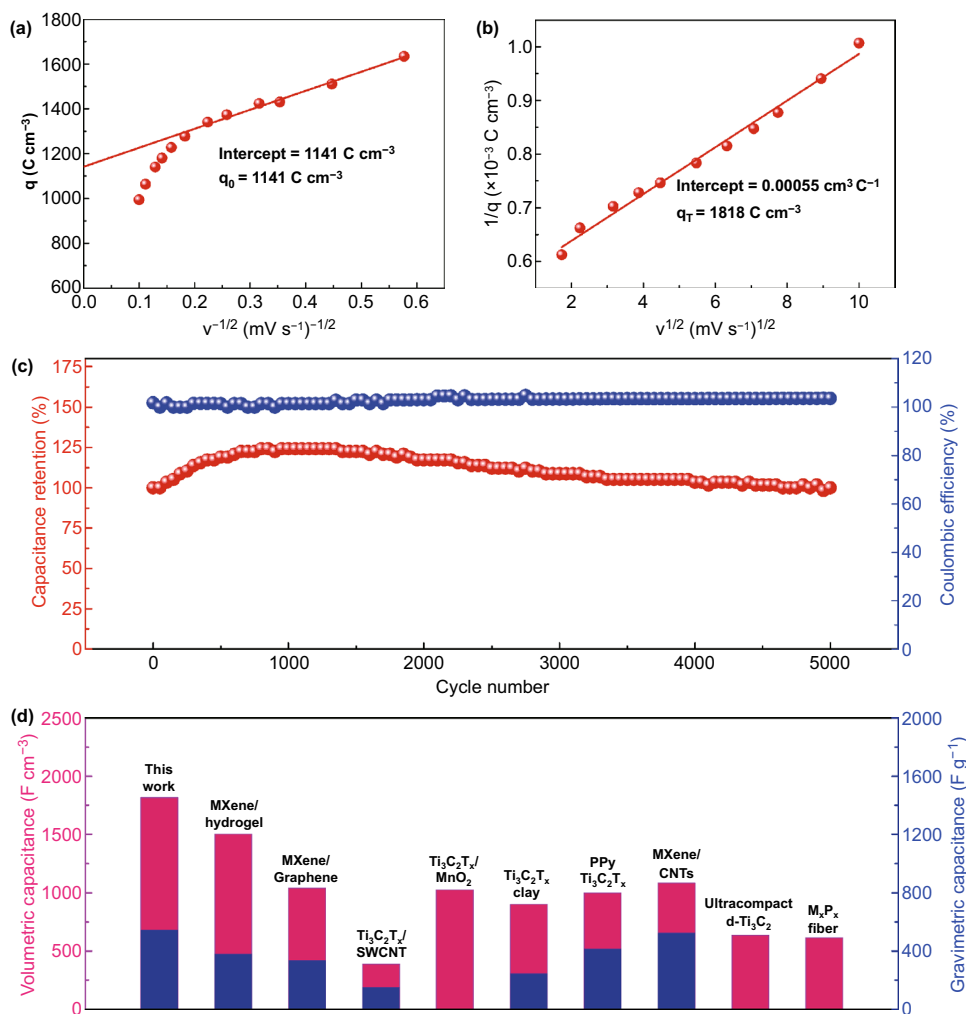


**Fig. 4** **a** Stored charges versus inverse of square root of the scan rates and **b** inverse of stored charges ( $q$ ) versus the square root of the scan rates according to the data from  $M/MoO_3$ -20% electrode, **c** cycling stability and Coulombic efficiency of the  $M/MoO_3$ -20% electrode at a current density of  $30 \text{ mA cm}^{-2}$  for 5000 cycles, **d** comparison of capacitance between the prepared  $M/MoO_3$ -20% electrode with previously reported state-of-the-art MXene-based electrodes

devices, a  $M/MoO_3$  symmetric supercapacitor was fabricated by employing two pieces of identical  $M/MoO_3$ -20% film electrode with a separator membrane in  $1 \text{ M H}_2\text{SO}_4$  aqueous electrolyte, which is illustrated in Fig. 5a. The CV curves of the symmetric supercapacitor at different scan rates are given in Fig. 5b. It can be observed that all the CV curves exhibit a pair of redox peaks in the voltage range of  $0\text{--}0.9 \text{ V}$  at the scan rate varying from  $10$  to  $200 \text{ mV s}^{-1}$ , demonstrating the predominant capacitance from redox pseudocapacitance. And the shape of redox peaks is still well maintained with a slight shift even when the scan rate reaches  $200 \text{ mV s}^{-1}$ , indicating good rate capability. For MXene symmetric supercapacitor, the CV curves exhibit a

pair of broader redox peaks at low scan rates (Fig. 5c). When the scan rates are increased to a high range, the redox peaks become more obscure especially in the discharging process. This indicates the  $M/MoO_3$  symmetric supercapacitor has different electrochemical processes compared with that of MXene symmetric supercapacitor. The specific capacitance of the symmetric device as a function of the scan rates is plotted in Fig. 5d, e based on the total active material. Notably, as expected,  $M/MoO_3$  symmetric supercapacitor exhibits an improved capacitive behavior. At the scan rate of  $10 \text{ mV s}^{-1}$ ,  $M/MoO_3$  symmetric supercapacitor has a capacitance of  $396 \text{ F cm}^{-3}$  ( $118.8 \text{ F g}^{-1}$ ), while MXene symmetric supercapacitor only exhibits a capacitance of  $297 \text{ F cm}^{-3}$

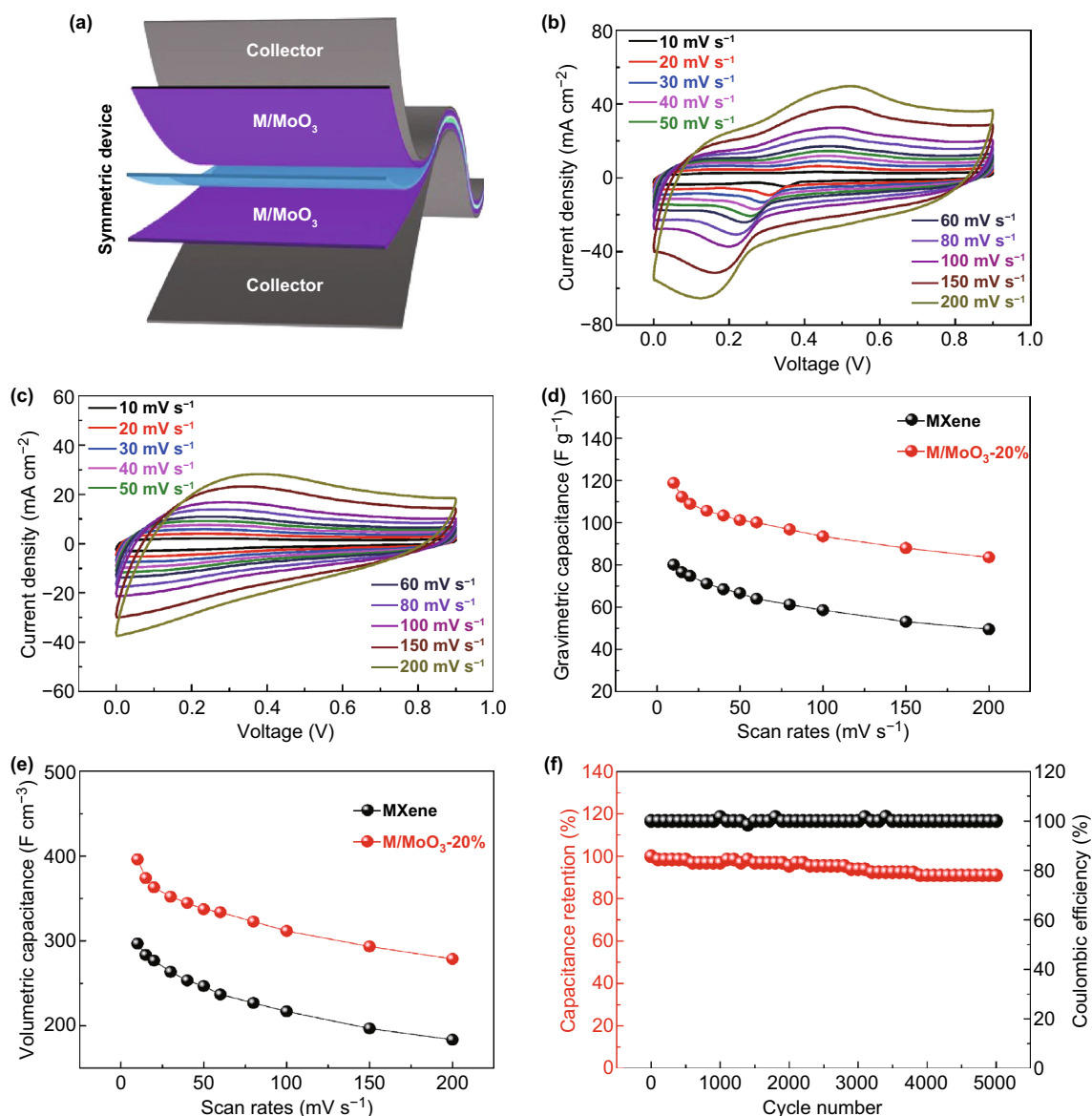


**Fig. 5** **a** Schematic representation of the assembled M/MoO<sub>3</sub> symmetric device, **b** CV curves of the symmetric supercapacitor based on the M/MoO<sub>3</sub>-20% electrodes at various scan rates, **c** CV curves of the MXene symmetric supercapacitor at various scan rates, **d** gravimetric and **e** volumetric specific capacitance of the symmetric supercapacitor, **f** cycling stability and Coulombic efficiency of the symmetric supercapacitor at a current density of 30 mA cm<sup>-2</sup> for 5000 cycles

(80.1 F g<sup>-1</sup>). With the scan rate increases to 200 mV s<sup>-1</sup>, a high capacitance retention of 70% is obtained for the M/MoO<sub>3</sub> symmetric supercapacitor, higher than that of MXene symmetric supercapacitor (62%), reflecting a great boost in capacitance and a high capacitance retention. In addition, the cyclic stability of M/MoO<sub>3</sub> symmetric supercapacitor was also tested with repeatedly being charged and discharged at a current density of 30 mA cm<sup>-2</sup>, as given in Fig. 5f. It shows that our device exhibits good cycling performance with a

capacitance retention of 90% of the initial available specific capacitance after 5000 cycles.

Benefiting from the high capacitance performance, the M/MoO<sub>3</sub> symmetric supercapacitor delivers a maximum energy density of 13.4 Wh kg<sup>-1</sup> at a power density of 534.6 W kg<sup>-1</sup>, much higher than that of MXene symmetric supercapacitor (9.0 Wh kg<sup>-1</sup> at a power density of 360.5 W kg<sup>-1</sup>) and comparable with other reported symmetric supercapacitors such as M/G-5% (10.5 Wh kg<sup>-1</sup>) [12],

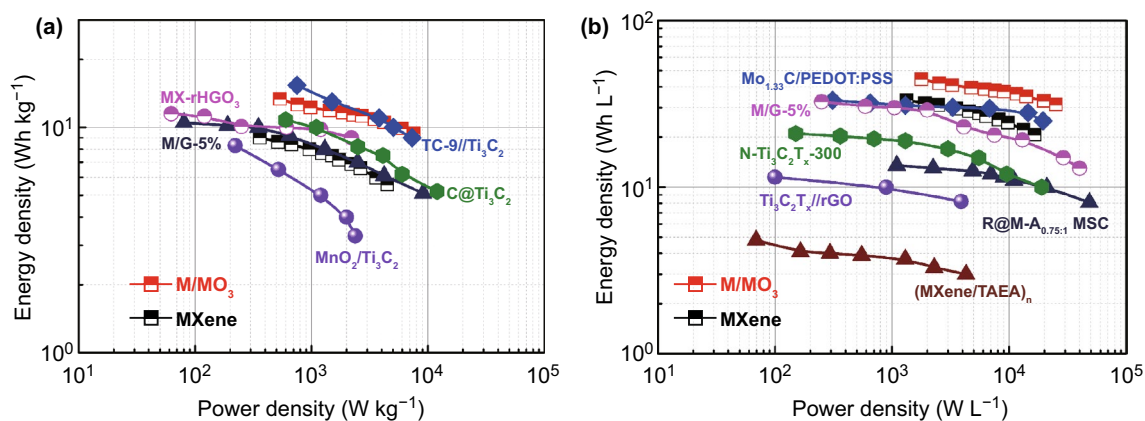


**Fig. 6** Ragone plots displaying energy and power densities of M/MoO<sub>3</sub> symmetric supercapacitor in comparison with other state-of-the-art MXene-based supercapacitors

MX-rHGO<sub>3</sub> (11.5 Wh kg<sup>-1</sup>) [36], C@Ti<sub>3</sub>C<sub>2</sub> (10.8 Wh kg<sup>-1</sup>) [37], MnO<sub>2</sub>/Ti<sub>3</sub>C<sub>2</sub> (8.3 Wh kg<sup>-1</sup>) [38] and even asymmetric TC-9//Ti<sub>3</sub>C<sub>2</sub> supercapacitor (15.4 Wh kg<sup>-1</sup>) [39], which is shown in Fig. 6. It is worth noting that the maximum volumetric energy density of M/MoO<sub>3</sub> symmetric supercapacitor can reach 44.6 Wh L<sup>-1</sup> at a power density of 1782 W L<sup>-1</sup> in sharp with that of MXene symmetric supercapacitors (33.4 Wh L<sup>-1</sup> at a power density of 1335 W L<sup>-1</sup>) and higher than those of previously reported state-of-the-art symmetric supercapacitors such as Mo<sub>1.33</sub>C MXene/PEDOT:PSS (33.2 Wh L<sup>-1</sup>) [40], Ti<sub>3</sub>C<sub>2</sub>T<sub>x</sub>/rGO-5 wt% (32.6 Wh L<sup>-1</sup>) [12], N-Ti<sub>3</sub>C<sub>2</sub>T<sub>x</sub>-300 (21 Wh L<sup>-1</sup>) [41], R@M-A<sub>0.75:1</sub> MSC (13.5 Wh L<sup>-1</sup>) [42], MXene/rGO (8.6 Wh L<sup>-1</sup>) [43] and (MXene/TAEA)<sub>n</sub> (5.1 Wh L<sup>-1</sup>) [22] (Table S2). Therefore, it is believed that this facile strategy by combining pseudocapacitive nanomaterials with MXene to improve the whole electrochemical performance and hold excellent flexibility of hybrid electrodes is considered be feasible for achieving high-energy-density flexible energy storage devices.

## 4 Conclusions

Ultrathin MoO<sub>3</sub> nanobelts and delaminated MXene nanosheets are integrated together by a facile and efficient vacuum-assisted method to fabricate all-pseudocapacitive and highly deformable M/MoO<sub>3</sub> hybrid films. The excellent synergetic effect is achieved in acidic electrolyte where MXene nanosheets can express highest pseudocapacitance. In the hybrid structure, MoO<sub>3</sub> nanobelts not only serve as the intercalators for the full advantage of MXene active surface

but also provide additional pseudocapacitance for the whole high capacitance performance. Meanwhile, MXene is an excellent conductive material to lower the intrinsic resistance of MoO<sub>3</sub> nanobelts for fast electron transport, thereby obtaining good rate capability. As a consequence, the as-prepared freestanding M/MoO<sub>3</sub>-20% hybrid film demonstrates an ultrahigh volumetric capacitance of 1817 F cm<sup>-3</sup> (545 F g<sup>-1</sup>), almost 1.5 times higher than that of pure MXene film, and exceeds large majority of previously reported MXene-based flexible electrodes. Due to ultrathin feature of both MoO<sub>3</sub> nanobelts and MXene nanosheets, outstanding flexibility is presented, which is bended, curled and even folded without cracks. Furthermore, the assembled symmetric supercapacitor device can obtain an excellent energy density of 44.6 Wh L<sup>-1</sup> (13.4 Wh kg<sup>-1</sup>) at a power density of 1782 W L<sup>-1</sup> in sharp with that of MXene symmetric supercapacitors (33.4 Wh L<sup>-1</sup> at a power density of 1335 W L<sup>-1</sup>) in aqueous electrolyte. We believe that the work would facilitate the progress of MXene-based flexible electrodes in achieving high-energy-density energy storage devices.

**Acknowledgements** This work was supported by Major Science and Technology Projects of Heilongjiang Province (2019ZX09A01); National Key Technology R&D Program (Grant No. 2017YFB1401805); the China Postdoctoral Science Foundation (2019T120285, 2018M641884); and Heilongjiang Province Postdoctoral Science Foundation (LBH-Z18235).

**Open Access** This article is licensed under a Creative Commons Attribution 4.0 International License, which permits use, sharing, adaptation, distribution and reproduction in any medium or format,

as long as you give appropriate credit to the original author(s) and the source, provide a link to the Creative Commons licence, and indicate if changes were made. The images or other third party material in this article are included in the article's Creative Commons licence, unless indicated otherwise in a credit line to the material. If material is not included in the article's Creative Commons licence and your intended use is not permitted by statutory regulation or exceeds the permitted use, you will need to obtain permission directly from the copyright holder. To view a copy of this licence, visit <http://creativecommons.org/licenses/by/4.0/>.

**Electronic supplementary material** The online version of this article (<https://doi.org/10.1007/s40820-020-00450-0>) contains supplementary material, which is available to authorized users.

## References

1. L. Yu, L. Hu, B. Anasori, Y.-T. Liu, Q. Zhu, P. Zhang, Y. Gogotsi, B. Xu, MXene-bonded activated carbon as a flexible electrode for high-performance supercapacitors. *ACS Energy Lett.* **3**(7), 1597–1603 (2018). <https://doi.org/10.1021/acsenenergylett.8b00718>
2. M. Boota, Y. Gogotsi, MXene-conducting polymer asymmetric pseudocapacitors. *Adv. Energy Mater.* **9**(7), 1802917 (2019). <https://doi.org/10.1002/aenm.201802917>
3. M.R. Lukatskaya, S. Kota, Z. Lin, M.-Q. Zhao, N. Shpigel et al., Ultra-high-rate pseudocapacitive energy storage in two-dimensional transition metal carbides. *Nat. Energy* **2**(8), 17105 (2017). <https://doi.org/10.1038/nenergy.2017.105>
4. C. Zhang, S.-H. Park, A. Seral-Ascaso, S. Barwich, N. McEvoy et al., High capacity silicon anodes enabled by MXene viscous aqueous ink. *Nat. Commun.* **10**(1), 849 (2019). <https://doi.org/10.1038/s41467-019-08383-y>
5. H. Tang, W. Li, L. Pan, C.P. Cullen, Y. Liu et al., In situ formed protective barrier enabled by sulfur@titanium carbide (MXene) ink for achieving high-capacity, long lifetime Li-S batteries. *Adv. Sci.* **5**(9), 1800502 (2018). <https://doi.org/10.1002/advs.201800502>
6. S. Zheng, C. Zhang, F. Zhou, Y. Dong, X. Shi, V. Nicolosi, Z.-S. Wu, X. Bao, Ionic liquid pre-intercalated MXene films for ionogel-based flexible micro-supercapacitors with high volumetric energy density. *J. Mater. Chem. A* **7**(16), 9478–9485 (2019). <https://doi.org/10.1039/c9ta02190f>
7. M. Alhabeb, K. Maleski, B. Anasori, P. Lelyukh, L. Clark, S. Sin, Y. Gogotsi, Guidelines for synthesis and processing of two-dimensional titanium carbide ( $\text{Ti}_3\text{C}_2\text{T}_x$  MXene). *Chem. Mater.* **29**(18), 7633–7644 (2017). <https://doi.org/10.1021/acs.chemmater.7b02847>
8. W. Cao, C. Ma, S. Tan, M. Ma, P. Wan, F. Chen, Ultrathin and flexible CNTs/MXene/cellulose nanofibrils composite paper for electromagnetic interference shielding. *Nano-Micro Lett.* **11**(1), 72 (2019). <https://doi.org/10.1007/s40820-019-0304-y>
9. S. Wang, Q. Wang, W. Zeng, M. Wang, L. Ruan, Y. Ma, A new free-standing aqueous zinc-ion capacitor based on  $\text{MnO}_2$ -CNTs cathode and MXene anode. *Nano-Micro Lett.* **11**(1), 70 (2019). <https://doi.org/10.1007/s40820-019-0301-1>
10. J. Pang, R.G. Mendes, A. Bachmatiuk, L. Zhao, H.Q. Ta et al., Applications of 2D MXenes in energy conversion and storage systems. *Chem. Soc. Rev.* **48**(1), 72–133 (2019). <https://doi.org/10.1039/c8cs00324f>
11. Y. Deng, T. Shang, Z. Wu, Y. Tao, C. Luo et al., Fast gelation of  $\text{Ti}_3\text{C}_2\text{T}_x$  MXene initiated by metal ions. *Adv. Mater.* **31**(43), 1902432 (2019). <https://doi.org/10.1002/adma.201902432>
12. J. Yan, C.E. Ren, K. Maleski, C.B. Hatter, B. Anasori, P. Urbankowski, A. Sarycheva, Y. Gogotsi, Flexible MXene/graphene films for ultrafast supercapacitors with outstanding volumetric capacitance. *Adv. Funct. Mater.* **27**(30), 1701264 (2017). <https://doi.org/10.1002/adfm.201701264>
13. M.Q. Zhao, C.E. Ren, Z. Ling, M.R. Lukatskaya, C. Zhang, K.L. Van Aken, M.W. Barsoum, Y. Gogotsi, Flexible MXene/carbon nanotube composite paper with high volumetric capacitance. *Adv. Mater.* **27**(2), 339–345 (2015). <https://doi.org/10.1002/adma.201404140>
14. Y. Wang, X. Wang, X. Li, Y. Bai, H. Xiao, Y. Liu, R. Liu, G. Yuan, Engineering 3D ion transport channels for flexible MXene films with superior capacitive performance. *Adv. Funct. Mater.* **29**(14), 1900326 (2019). <https://doi.org/10.1002/adfm.201900326>
15. Z. Ling, C.E. Ren, M.-Q. Zhao, J. Yang, J.M. Giammarco, J. Qiu, M.W. Barsoum, Y. Gogotsi, Flexible and conductive MXene films and nanocomposites with high capacitance. *Proc. Natl. Acad. Sci. U.S.A.* **111**(47), 16676–16681 (2014). <https://doi.org/10.1073/pnas.1414215111>
16. Y. Wang, H. Dou, J. Wang, B. Ding, Y. Xu, Z. Chang, X. Hao, Three-dimensional porous MXene/layered double hydroxide composite for high performance supercapacitors. *J. Power Sources* **327**, 221–228 (2016). <https://doi.org/10.1016/j.jpowsour.2016.07.062>
17. R. Zhao, M. Wang, D. Zhao, H. Li, C. Wang, L. Yin, Molecular-level heterostructures assembled from titanium carbide MXene and Ni-Co-Al layered double-hydroxide nanosheets for all-solid-state flexible asymmetric high-energy supercapacitors. *ACS Energy Lett.* **3**(1), 132–140 (2017). <https://doi.org/10.1021/acsenenergylett.7b01063>
18. J. Zhou, J. Yu, L. Shi, Z. Wang, H. Liu et al., A conductive and highly deformable all-pseudocapacitive composite paper as supercapacitor electrode with improved areal and volumetric capacitance. *Small* **14**(51), 1803786 (2018). <https://doi.org/10.1002/sml.201803786>
19. F. Li, Y.-L. Liu, G.-G. Wang, H.-Y. Zhang, B. Zhang et al., Few-layered  $\text{Ti}_3\text{C}_2\text{T}_x$  MXenes coupled with  $\text{Fe}_2\text{O}_3$  nanorod arrays grown on carbon cloth as anodes for flexible asymmetric supercapacitors. *J. Mater. Chem. A* **7**(39), 22631–22641 (2019). <https://doi.org/10.1039/c9ta08144e>
20. Q.-L. Wu, S.-X. Zhao, L. Yu, X.-X. Zheng, Y.-F. Wang, L.-Q. Yu, C.-W. Nan, G. Cao, Oxygen vacancy-enriched  $\text{MoO}_{3-x}$  nanobelts for asymmetric supercapacitors with excellent



- room/low temperature performance. *J. Mater. Chem. A* **7**(21), 13205–13214 (2019). <https://doi.org/10.1039/c9ta03471d>
21. K. Zhou, W. Zhou, X. Liu, Y. Sang, S. Ji et al., Ultrathin MoO<sub>3</sub> nanocrystals self-assembled on graphene nanosheets via oxygen bonding as supercapacitor electrodes of high capacitance and long cycle life. *Nano Energy* **12**, 510–520 (2015). <https://doi.org/10.1016/j.nanoen.2015.01.017>
  22. W. Tian, A. Vahid Mohammadi, Z. Wang, L. Ouyang, M. Beidaghi, M.M. Hamed, Layer-by-layer self-assembly of pillared two-dimensional multilayers. *Nat. Commun.* **10**(1), 2558 (2019). <https://doi.org/10.1038/s41467-019-10631-0>
  23. C.J. Zhang, B. Anasori, A. Seral-Ascaso, S.H. Park, N. McEvoy et al., Transparent, flexible, and conductive 2D titanium carbide (MXene) films with high volumetric capacitance. *Adv. Mater.* **29**(36), 1702678 (2017). <https://doi.org/10.1002/adma.201702678>
  24. X. Zhang, Q. Fu, H. Huang, L. Wei, X. Guo, Silver-quantum-dot-modified MoO<sub>3</sub> and MnO<sub>2</sub> paper-like freestanding films for flexible solid-state asymmetric supercapacitors. *Small* **15**(13), 1805235 (2019). <https://doi.org/10.1002/sml.201805235>
  25. J. Yang, X. Xiao, P. Chen, K. Zhu, K. Cheng et al., Creating oxygen-vacancies in MoO<sub>3-x</sub> nanobelts toward high volumetric energy-density asymmetric supercapacitors with long lifespan. *Nano Energy* **58**, 455–465 (2019). <https://doi.org/10.1016/j.nanoen.2019.01.071>
  26. B. Yao, L. Huang, J. Zhang, X. Gao, J. Wu et al., Flexible transparent molybdenum trioxide nanopaper for energy storage. *Adv. Mater.* **28**(30), 6353–6358 (2016). <https://doi.org/10.1002/adma.201600529>
  27. Y. Chen, T. Zhou, L. Li, W.K. Pang, X. He, Y.N. Liu, Z. Guo, Interfacial engineering of nickel boride/metaborate and its effect on high energy density asymmetric supercapacitors. *ACS Nano* **13**(8), 9376–9385 (2019). <https://doi.org/10.1021/acsnano.9b04005>
  28. J. Hao, J. Zhang, G. Xia, Y. Liu, Y. Zheng et al., Heterostructure manipulation via in situ localized phase transformation for high-rate and highly durable lithium ion storage. *ACS Nano* **12**(10), 10430–10438 (2018). <https://doi.org/10.1021/acsnano.8b06020>
  29. H. He, D. Huang, Q. Gan, J. Hao, S. Liu et al., Anion vacancies regulating endows MoSSe with fast and stable potassium ion storage. *ACS Nano* **13**(10), 11843–11852 (2019). <https://doi.org/10.1021/acsnano.9b05865>
  30. M. Hu, C. Cui, C. Shi, Z.S. Wu, J. Yang et al., High-energy-density hydrogen-ion-rocking-chair hybrid supercapacitors based on Ti<sub>3</sub>C<sub>2</sub>T<sub>x</sub> MXene and carbon nanotubes mediated by redox active molecule. *ACS Nano* **13**(6), 6899–6905 (2019). <https://doi.org/10.1021/acsnano.9b01762>
  31. M. Ghidui, M.R. Lukatskaya, M.Q. Zhao, Y. Gogotsi, M.W. Barsoum, Conductive two-dimensional titanium carbide ‘clay’ with high volumetric capacitance. *Nature* **516**(7529), 78–81 (2014). <https://doi.org/10.1038/nature13970>
  32. M. Boota, B. Anasori, C. Voigt, M.Q. Zhao, M.W. Barsoum, Y. Gogotsi, Pseudocapacitive electrodes produced by oxidant-free polymerization of pyrrole between the layers of 2D titanium carbide (MXene). *Adv. Mater.* **28**(7), 1517–1522 (2016). <https://doi.org/10.1002/adma.201504705>
  33. Z. Wang, S. Qin, S. Seyedin, J. Zhang, J. Wang et al., High-performance biscrolled MXene/carbon nanotube yarn supercapacitors. *Small* **14**(37), 1802225 (2018). <https://doi.org/10.1002/sml.201802225>
  34. C. Yang, Y. Tang, Y. Tian, Y. Luo, Y. He, X. Yin, W. Que, Achieving of flexible, free-standing, ultracompact delaminated titanium carbide films for high volumetric performance and heat-resistant symmetric supercapacitors. *Adv. Funct. Mater.* **28**(15), 1705487 (2018). <https://doi.org/10.1002/adfm.201705487>
  35. J. Zhang, S. Seyedin, S. Qin, Z. Wang, S. Moradi et al., Highly conductive Ti<sub>3</sub>C<sub>2</sub>T<sub>x</sub> MXene hybrid fibers for flexible and elastic fiber-shaped supercapacitors. *Small* **15**(8), 1804732 (2019). <https://doi.org/10.1002/sml.201804732>
  36. Z. Fan, Y. Wang, Z. Xie, D. Wang, Y. Yuan et al., Modified MXene/holey graphene films for advanced supercapacitor electrodes with superior energy storage. *Adv. Sci.* **5**(10), 1800750 (2018). <https://doi.org/10.1002/advs.201800750>
  37. Z. Pan, X. Ji, Facile synthesis of nitrogen and oxygen co-doped C@ Ti<sub>3</sub>C<sub>2</sub> MXene for high performance symmetric supercapacitors. *J. Power Sources* **439**, 227068 (2019). <https://doi.org/10.1016/j.jpowsour.2019.227068>
  38. W. Liu, Z. Wang, Y. Su, Q. Li, Z. Zhao, F. Geng, Molecularly stacking manganese dioxide/titanium carbide sheets to produce highly flexible and conductive film electrodes with improved pseudocapacitive performances. *Adv. Energy Mater.* **7**(22), 1602834 (2017). <https://doi.org/10.1002/aenm.201602834>
  39. Z. Pan, F. Cao, X. Hu, X. Ji, A facile method for synthesizing Cu decorated Ti<sub>3</sub>C<sub>2</sub> MXene with enhanced performance for asymmetric supercapacitors. *J. Mater. Chem. A* **7**(15), 8984–8992 (2019). <https://doi.org/10.1039/c9ta00085b>
  40. L. Qin, Q. Tao, A. El Ghazaly, J. Fernandez-Rodriguez, P.O. Å. Persson, J. Rosen, F. Zhang, High-performance ultrathin flexible solid-state supercapacitors based on solution processable Mo<sub>1.33</sub>C MXene and PEDOT:PSS. *Adv. Funct. Mater.* **28**(2), 1703808 (2018). <https://doi.org/10.1002/adfm.201703808>
  41. Y. Tian, W. Que, Y. Luo, C. Yang, X. Yin, L.B. Kong, Surface nitrogen-modified 2D titanium carbide (MXene) with high energy density for aqueous supercapacitor applications. *J. Mater. Chem. A* **7**(10), 5416–5425 (2019). <https://doi.org/10.1039/c9ta00076c>
  42. H. Li, X. Li, J. Liang, Y. Chen, Hydrous RuO<sub>2</sub>-decorated mxene coordinating with silver nanowire inks enabling fully printed micro-supercapacitors with extraordinary volumetric performance. *Adv. Energy Mater.* **9**(15), 1803987 (2019). <https://doi.org/10.1002/aenm.201803987>
  43. C. Couly, M. Alhabeab, K.L. Van Aken, N. Kurra, L. Gomes et al., Asymmetric flexible MXene-reduced graphene oxide micro-supercapacitor. *Adv. Electron. Mater.* **4**(1), 1700339 (2018). <https://doi.org/10.1002/aelm.201700339>